



**HAL**  
open science

## Estimation of Finescale Rainfall Fields Using Broadcast TV Satellite Links and a 4DVAR Assimilation Method

François Mercier, Laurent Barthès, Cécile Mallet

► **To cite this version:**

François Mercier, Laurent Barthès, Cécile Mallet. Estimation of Finescale Rainfall Fields Using Broadcast TV Satellite Links and a 4DVAR Assimilation Method. *Journal of Atmospheric and Oceanic Technology*, 2015, 32 (10), pp.1709-1728. 10.1175/JTECH-D-14-00125.1 . insu-01157488

**HAL Id: insu-01157488**

**<https://insu.hal.science/insu-01157488>**

Submitted on 26 Oct 2015

**HAL** is a multi-disciplinary open access archive for the deposit and dissemination of scientific research documents, whether they are published or not. The documents may come from teaching and research institutions in France or abroad, or from public or private research centers.

L'archive ouverte pluridisciplinaire **HAL**, est destinée au dépôt et à la diffusion de documents scientifiques de niveau recherche, publiés ou non, émanant des établissements d'enseignement et de recherche français ou étrangers, des laboratoires publics ou privés.

## Estimation of Finescale Rainfall Fields Using Broadcast TV Satellite Links and a 4DVAR Assimilation Method

FRANÇOIS MERCIER, LAURENT BARTHÈS, AND CÉCILE MALLET

*Université de Versailles Saint-Quentin-en-Yveline, Versailles, and Sorbonne Universités, UPMC University Paris 06, Paris, and CNRS/INSU, LATMOS-IPSL, Guyancourt, France*

(Manuscript received 22 May 2014, in final form 23 April 2015)

### ABSTRACT

This study proposes a method based on the use of a set of commercial satellite-to-Earth microwave links to rebuild finescale rainfall fields. Such microwave links exist all over the world and can be used to estimate the integrated rain attenuation over the links' first 5–7 km with a very high temporal resolution (10 s in the present case). The retrieval algorithm makes use of a four-dimensional variational data assimilation (4DVAR) method involving a numerical advection scheme. The advection velocity is recovered from the observations or from radar rainfall fields at successive time steps.

This technique has been successively applied to simulated 2D rain maps and to real data recorded in the autumn of 2013 during the Hydrological Cycle in the Mediterranean Experiment (HyMeX), with one sensor receiving microwave signals from four different satellites. The performance of this system is assessed and is compared to an operational Météo-France radar and a network of 10 rain gauges. Because of the limitations of the propagation model, this study is limited to the events with strong advective characteristics (four out of eight recorded events). For these events (only), the method produces rainfall fields that are highly correlated with the radar maps at spatial resolutions greater than  $2 \times 2 \text{ km}^2$ . The point-scale results are also satisfactory for temporal resolutions greater than 10 min (mean correlation with rain gauge data equal to approximately 0.8, similar to the correlation between radar and rain gauge data).

This method can also be adapted to the fusion of a rain gauge with microwave link measurements and, through the use of several sensors, it has the potential of being applied to larger areas.

### 1. Introduction

The estimation of small-scale rainfall is an important issue in several domains, such as urban hydrology, flash-flood forecasting, water cycle studies, or climate change. Rain gauge networks or weather radars are commonly used for the observation of rain cells. The latter system allows large areas to be observed from one site with a typical temporal resolution of 5–15 min and a spatial resolution of  $1 \text{ km}^2$ . Rain gauge systems have a temporal resolution in the range between 5 min and 1 day and require a large number of rain gauges in order to achieve good spatial sampling. Both techniques have various disadvantages, such as the cost of weather radars and the cost of maintaining a large number of rain gauges.

Microwaves are affected by rain, especially at frequencies above 10 GHz. Their specific attenuation

$K$  ( $\text{dB km}^{-1}$ ) can be related to the rainfall rate  $R$  ( $\text{mm h}^{-1}$ ) by the well-known power-law equation

$$K = aR^b, \quad (1)$$

where  $a$  and  $b$  are two parameters depending on the frequency, the polarization, and the drop size distribution (see, e.g., [Leijnse et al. 2008](#)).

Several studies have evaluated the accuracy with which localized or integrated rainfall rates can be derived from satellite-to-Earth attenuation data (see, for instance, [Maitra and Chakravarty 2005](#)) and have explored various applications of this technique, often using cellular communication networks ([Schleiss and Berne 2010](#); [Chwala et al. 2012](#); [Overeem et al. 2013](#)). In addition, a considerable number of studies have investigated the reconstruction of rainfall fields from microwave attenuation measurements. These studies make use of both simulated data ([Giuli et al. 1991, 1999](#)), with a predefined chosen geometry, and real data ([Overeem et al. 2013](#); [Zinevich et al. 2009](#)) provided by

---

*Corresponding author address:* François Mercier, LATMOS, 11 Boulevard d'Alembert, 78280 Guyancourt, France.  
E-mail: francois.mercier@latmos.ipsl.fr

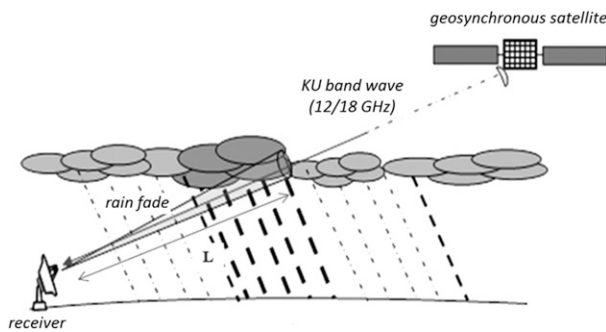


FIG. 1. Measurement setup used for the experiments described in this paper. A receiver on the ground measures Ku-band microwave signals transmitted by a geosynchronous satellite, and a spectrum analyzer determines the rain-induced attenuation of the recorded signals. See [Barthès and Mallet \(2013\)](#) for further details.

cellular communication networks. The reconstruction of rainfall fields from microwave attenuation data employs various techniques, such as tomography ([Giuli et al. 1991](#); [Zinevich et al. 2008](#)) and ordinary kriging ([Overeem et al. 2013](#)). [Zinevich et al. \(2009\)](#) first uses a data assimilation technique (extended Kalman filter) based on a rainfall advection model.

The present study differs from previous research in this field with respect to two major aspects of the data retrieval and processing. First, we use attenuation measurements performed on a set of geostationary broadcast television (TV) satellites. These allow the integrated rain attenuation to be estimate along the link's first 5–7 km [depending on the freezing level and the direction (azimuth and elevation) in which the satellite is viewed from the receiver] with a high temporal resolution. This measurement system is presented in detail in [Barthès and Mallet \(2013\)](#) and schematically in [Fig. 1](#). Second, the retrieval algorithm is based on the four-dimensional variational data assimilation (4DVAR) of observations in an advection model (see [section 3](#)).

In this paper, we use data recorded in the southeastern area of France, in the Cévennes–Vivarais region, during the extreme meteorological events that occurred in 2013 in the context of the Hydrological Cycle in the Mediterranean Experiment (HyMeX; see, for instance, [Drobinski et al. 2013](#)). The measuring device comprises a single receiver and four low-noise block downconverters mounted on a multifocus antenna, allowing quasi-instantaneous attenuation measurements along four azimuths corresponding to the positions of four TV satellites operating in the Ku band (12 GHz). By using just one receiver to measure the signals from four satellite links (satlinks), the spatial sampling of the rainfall is very sparse. Conversely, this device has a very good temporal resolution (10 s), and it is thus possible to rebuild rainfall fields from these measurements and then to connect the measurements

recorded at successive discrete time steps through the use of an advection model to propagate the rainfall fields. A simple triangulation algorithm was developed to deduce the direction and speed of advection from the measurements. The rainfall field is then determined with a spatiotemporal resolution of  $0.5 \times 0.5 \text{ km}^2$  and 10 s, based on a combination of measurements and values retrieved from the advection model with the 4DVAR algorithm. The performance of the measurement system and its associated retrieval algorithm is assessed and compared with radar and rain gauge observations.

The datasets are described in [section 2](#). We then present the retrieval algorithm in [section 3](#). [Section 4](#) describes the algorithm developed to compute the advection velocity and the simulated data used to evaluate its performance. In [section 5](#) we provide initial results and estimate our model's performance through the use of simulated data. Finally, [section 6](#) presents the results obtained with several case studies, using real measurements recorded during rainfall events. [Section 7](#) provides our conclusions.

## 2. Datasets

In this section, we first present the studied area, its location, and principal characteristics, as well as the size and features of the attenuation measuring device. We then present the radar and rain gauge data used to validate the method.

The Ku receiver is located at Mirabel, in the Ardèche department of the southwestern area of France. Mirabel is situated in a mountainous area called the Cévennes–Vivarais (see [Fig. 2](#)). This region experiences intense Mediterranean rain events with strong spatial and temporal variabilities, which are amplified by the mountainous topography. A description of the region and its characteristics is provided in [Delrieu et al. \(2009\)](#) and [Molinié et al. \(2012\)](#). The Ku sensor can record four different satellite-to-Earth microwave links simultaneously. The data made available for our study span several different time periods in 2013. The characteristics (azimuth and elevation) of the microwave links are provided in [Table 1](#). As described above (see [section 1](#); [Fig. 1](#)), the effective pathlengths depend on the altitude of the freezing level, which is calculated using the temperature recorded at Météo-France's Aubenas weather station, located 9 km to the west of the sensor, and assuming a temperature decrease of  $1^\circ\text{C}$  every 150 m. As none of the studied events was observed in winter, the freezing level could be considered to be consistently higher than 2.5 km. The length of the link is thus given by  $H_0/\tan(\alpha)$ , where  $H_0$  is the freezing level and  $\alpha$  is the elevation angle. The link's pathlength thus has a minimum value of 4 km and can exceed 7 km during warm-rain events.

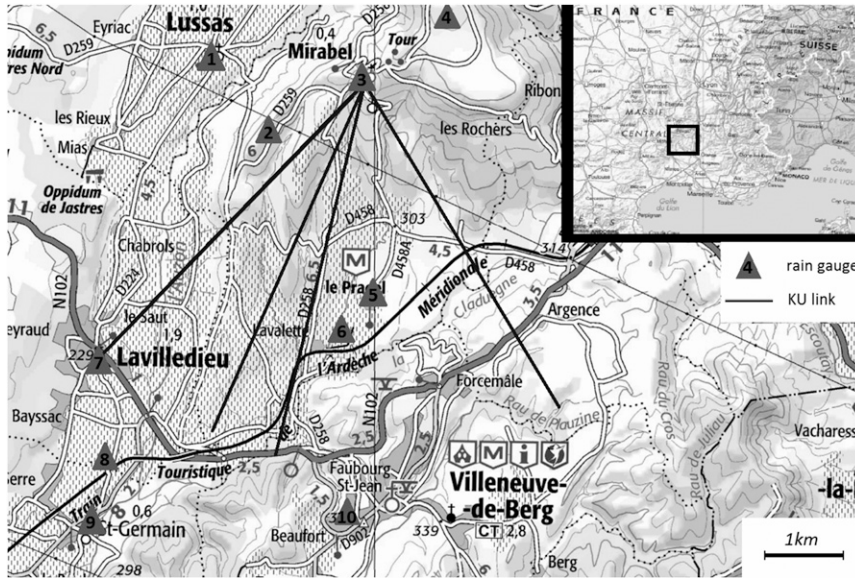


FIG. 2. Location of the measuring devices used during our experiments in 2013. The black frame indicates the position of the working area (Cévennes–Vivarais region) in the south of France. The enlarged section of this map (approximately 10 km in the east–west direction) indicates the location and geometry of the monitored Ku-band links (black lines) and of the HPiconet network rain gauges (gray triangles) used to validate the model. The pathlength of the microwave links is approximately 5 km.

The retrieval method described here was validated using two different rain measurement systems: weather radar and rain gauges. The Météo-France radar situated at Bollène, 40 km from the sensor, provided us with rainfall fields with a spatial resolution of  $1 \times 1 \text{ km}^2$  and a temporal resolution of 5 min. The radar data were processed as described by Tabary (2007) and were then used to assess the performance of our technique, especially for space- and time-integrated quantities.

The rain gauge data are provided by the HPiconet network (<http://www.ohmcv.fr/hpiconet/index.html>), developed by the Observatoire Hydro-Météorologique Méditerranéen Cévennes–Vivarais (OHMCV) and HyMeX. This network comprises 10 rain gauges covering the same surface area as that analyzed by the Ku links, which was equal to approximately  $60 \text{ km}^2$ . The locations of these rain gauges are shown in Fig. 2. Their temporal resolution is 5 min. The data from these gauges were used to validate our field rebuilding method at certain points and to determine the Ku data integration times required to obtain sufficiently accurate rainfall values for point-scale locations.

### 3. Retrieval algorithm

In this section we describe the algorithm used to rebuild the rainfall fields. First, we present the numerical

model used to propagate the rainfall fields. Then, we describe the 4DVAR data assimilation algorithm developed for this application.

#### a. Space–time direct model

To simplify the description of the spatial dynamics of rainfall, an advection model is used to propagate the rainfall fields. The aim is not to physically describe the atmospheric phenomena, since the conserved properties that are generally advected are heat or humidity (Allen et al. (1991)), but to describe the evolution of the rainfall cells during short periods of time (less than 45 min). This approach to the modeling of the transport of rainfall fields has already been applied and discussed in Zinevich et al. (2009). Diffusion is not taken into account for two main reasons: first, the network of satellite links is not

TABLE 1. Azimuth and elevation angles of the Ku-band microwave links observed during rain field experiments in the south-western area of France in 2013. The link numbers correspond to those indicated in Fig. 2.

2013 events		
Link number (from west to east)	Azimuth	Elev angle
1	223.8°	28.5°
2	203.5°	35.9°
3	193.4°	37.7°
4	148.2°	33.5°

sufficiently dense to provide a satisfactory estimation of the diffusion parameters; second, we made our analyses over short time periods, during which the rainfall cells were assumed to remain relatively underformed (the consequences of this hypothesis are discussed in section 6).

Three important hypotheses are made.

- (i) Contrary to Zinevich et al. (2009), we work directly with specific attenuations, rather than rainfall rates ( $\text{mm h}^{-1}$ ) in order to simplify the observation operator. The specific attenuations are then converted into rainfall rates using Eq. (1) at the very end of the process.
- (ii) The analysis is performed in two dimensions, meaning that measurements made at ground level (horizontal projection of the links path) are considered. This implies the assumption of vertical homogeneity of the rain field.
- (iii) In all of our experiments, the wind vector field over the working area ( $29 \text{ km} \times 29 \text{ km}$ ) is assumed to be constant over time and homogeneous in space during the displacement of the rain cell across the observation area. Although the theoretical assimilation algorithm remains operational with a variable wind field, our measurement network is too sparse to evaluate such a field. For an area with a steep topography, as in the Cévennes, this hypothesis is reasonable for brief events only. For this reason, our analyses of rainfall events were restricted to short periods only (less than 45 min). For longer durations the events were split into several distinct parts (each part being treated as an independent event with, for instance, its own advection velocity).

The advection equation for a specific attenuation field  $K(t, x, y)$  is given by

$$\frac{\partial K}{\partial t} = u \frac{\partial K}{\partial x} + v \frac{\partial K}{\partial y}, \quad (2)$$

where  $u$  and  $v$  denote the two horizontal components of the wind.

To discretize Eq. (2), we use the finite difference scheme developed by Smolarkiewicz (1983). The rain fields generally have a strong spatial variability, especially in mountainous areas such as the Cévennes–Vivarais region (see, e.g., Delrieu et al. 2009). To conserve the strong rainfall gradients when the fields are propagated through time by the numerical advection scheme, a scheme without strong numerical diffusion is needed. The Smolarkiewicz scheme, developed for the modeling of atmospheric phenomena, has this characteristic.

In the present study, although their values are not critical, the parameters of the Smolarkiewicz (1983)

scheme  $Sc$  and  $\epsilon$  [see Eqs. (15) and (23) in Smolarkiewicz 1983] are set to 1.04 and  $10^{-15}$ , respectively.

The stability condition for this scheme (Courant–Friedrichs–Lewy condition) takes the form

$$\Delta t \sqrt{\frac{u^2}{\Delta x^2} + \frac{v^2}{\Delta y^2}} < \frac{1}{\sqrt{2}}, \quad (3)$$

where  $(\Delta x, \Delta y)$  is the spatial resolution and  $\Delta t$  is the temporal resolution.

In our experiments on real data, we work with a 1-s time step and with a spatial resolution of  $0.5 \text{ km} \times 0.5 \text{ km}$ . These parameters respect Eq. (3) for wind velocities up to  $350 \text{ m s}^{-1}$ .

#### b. 4DVAR data assimilation

In this section, we briefly recall the principles of the 4DVAR. We then develop the cost function used in this paper and include the filter term to ensure that the rebuilt rainfall fields are realistic. Finally, we present the YAO software used to implement the assimilation algorithm.

##### 1) 4DVAR THEORY

Variational data assimilation consists of minimizing a cost function depending on an unknown initial field (and eventually on some model parameters). This function generally has two parts. The first part of these evaluates the gap between the available observations and the unknown initial field, propagated through time by a numerical model. The second part of the function evaluates the gap between the unknown initial field and a background field (first guess). Kalnay (2003) presents the principles of variational data assimilation. Navon (2009) presents a history of data assimilation and a review of the variational assimilation methods, including 4DVAR. Figure 3 presents the different steps of the assimilation algorithm developed in this study.

The specific attenuation field at time  $t_0 = 0$  is noted  $\mathbf{x}^0$ . The unknown field at time  $t_n = n\Delta t$  is  $\mathbf{x}^n = \mathbf{x}(t_n)$ , and the variable of the cost function (control parameter), which is the initial field in this study, is  $\mathbf{x} = \mathbf{x}^0$ . The cost function thus has the form

$$J(\mathbf{x}) = J_o(\mathbf{x}) + J_b(\mathbf{x}) \quad (4)$$

with

$$J_b(\mathbf{x}) = \frac{1}{2} (\mathbf{x} - \mathbf{x}_b)^T \mathbf{B}^{-1} (\mathbf{x} - \mathbf{x}_b) \quad (5)$$

and

$$J_o(\mathbf{x}) = \frac{1}{2} \sum_{n=0}^N (\mathbf{y}^n - \mathbf{H}_n \mathbf{x}^n)^T \mathbf{R}_n^{-1} (\mathbf{y}^n - \mathbf{H}_n \mathbf{x}^n), \quad (6)$$

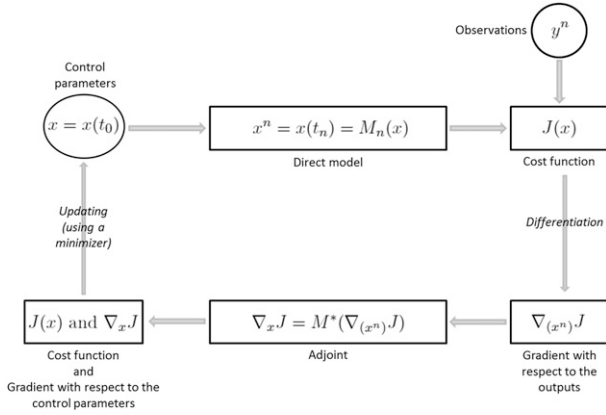


FIG. 3. Block diagram presenting the different steps of the 4DVAR algorithm described in section 3. The notations are the same as those used in this section.

where  $N\Delta t$  is the duration of the simulation,  $x_b$  is the background,  $\mathbf{B}$  is the background error covariance matrix,  $\mathbf{y}^n$  represents the observations available at time  $t_n$ ,  $\mathbf{R}_n$  is the observations' error covariance matrix, and  $\mathbf{H}_n$  is an operator used to project the field  $\mathbf{x}^n$  on the observation space at time  $t_n$ .

If the forecast model is assumed to be deterministic (which means that an initial field  $\mathbf{x}_0$  propagated by the model gives a unique field at time  $t_n$ ), with  $\mathbf{M}_{n-1,n}$  representing the forecast step propagating a field from time  $t_{n-1}$  to time  $t_n$  (the model being nonlinear), then we have

$$\mathbf{x}^n = \mathbf{M}_{n-1,n}(\mathbf{x}^{n-1}). \quad (7)$$

Then, noting  $\mathbf{M}_n = \mathbf{M}_{n-1,n} \circ \mathbf{M}_{n-2,n-1} \circ \dots \circ \mathbf{M}_{0,1}$ , we have

$$\mathbf{x}^n = \mathbf{M}_n(\mathbf{x}). \quad (8)$$

The gradient of the cost function (4) is then given by

$$\nabla J(x) = \mathbf{B}^{-1}(\mathbf{x} - \mathbf{x}_b) - \sum_{n=0}^N \mathbf{M}_n^T \mathbf{H}_n^T \mathbf{R}_n^{-1} [\mathbf{y}^n - \mathbf{H}_n \mathbf{M}_n(x)], \quad (9)$$

where  $\mathbf{M}_n^T$  is the adjoint of the linearized operator  $\mathbf{M}_n$ .

The difficulty in using the 4DVAR data assimilation method lies in the implementation of the adjoint model. In this study we use the YAO software developed by Laboratoire d'Océanographie et du Climat: Expérimentations et Approches Numériques (LOCEAN) and described in Nardi et al. (2009). This provides a simple method for deriving the adjoint. A brief description of this software is provided in section 3b(3).

## 2) COST FUNCTION

The background field  $\mathbf{x}_b$  is usually the analyzed state of a previous assimilation cycle. However, in this study,

as we work with very brief, highly variable events, the assumption is made that no background field is available. Moreover, a filter term  $J_f$  is added to the cost function in order to provide a certain degree of correlation between neighboring pixels, similarly to the approach of Giuli et al. (1991), that thus smooths the rainfall fields. This filter term is assumed to have the value 0 for a constant field. The cost function of the assimilation is then

$$J(\mathbf{x}) = J_o(\mathbf{x}) + J_f(\mathbf{x}). \quad (10)$$

The filter term  $J_f$  takes the form

$$J_f(\mathbf{x}) = c_f \|\mathbf{x} - \mathbf{m}\|^2, \quad (11)$$

where  $c_f$  is a scalar weighting coefficient and the vector  $\mathbf{m}$  at grid point  $(i, j)$  is the average value of the field around point  $(i, j)$ , namely,

$$m_{ij} = \frac{1}{9} \sum_{\substack{a=-1,0,1 \\ b=-1,0,1}} x_{i+a,j+b}, \quad (12)$$

where  $x_{i+a,j+b}$  is the component of the field  $x$  at point  $[(i+a)\Delta x, (j+b)\Delta y]$ .

It should be noted that  $J_f$  is a filter term, in the sense that its value increases when the gradients of the attenuation field increase. Its aim is to prevent the assimilation algorithm from producing physically incoherent attenuation fields (meaning, with excessively large values of attenuation or gradients). Also that  $J_f$  can be written in the assimilation formalism as  $J_f(\mathbf{x}) = \|\mathbf{x}\|_{\mathbf{B}^{-1}} = J_b(\mathbf{x})$ , where  $\|\mathbf{u}\|_{\mathbf{A}} = \mathbf{u}^T \mathbf{A} \mathbf{u}$ . This implies a background field  $\mathbf{x}_b$  of 0 and that a background error covariance matrix ensuring  $J_f(\mathbf{x})$  of 0 is obtained whenever  $\mathbf{x}$  is constant. The background error covariance matrix  $\mathbf{B}$ , such as  $c_f \|\mathbf{x} - \mathbf{m}\|^2 = \|\mathbf{x}\|_{\mathbf{B}^{-1}}$ , is given by  $\mathbf{B}^{-1} = \sum \mathbf{B}_k$ , where  $k$  represents one of the points of the discretized domain [one of the  $(i, j)$  points]. Then, as described in Giuli et al. (1991), the value of the matrix  $\mathbf{B}_k$  at grid point  $(i, j)$  (written  $b_{ij}^k$ ) is given by

$$b_{ij}^k = c_f \begin{cases} \frac{64}{81} & \text{if } k = (i, j) \\ -\frac{8}{81} & \text{if } k = (i, j \pm 1) \text{ or } k = (i \pm 1, j). \\ \frac{1}{81} & \text{if } k = (i \pm 1, j \pm 1) \end{cases} \quad (13)$$

## 3) THE YAO SOFTWARE

The YAO software was developed by LOCEAN to assist with the implementation of the adjoint model for

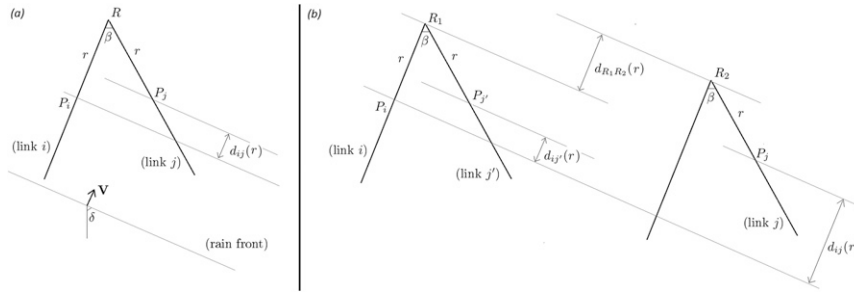


FIG. 4. (a) Notations used in section 4b, defining the distance  $d_{ij}(r)$  between two points  $P_i$  and  $P_j$  on satellite links  $i$  and  $j$ , at a distance  $r$  from receiver  $R$ . The vector  $\mathbf{V}$  defines the advection velocity (velocity of the rain cell), defined by its norm  $V$  and argument  $\delta$ . The angle  $\beta$  is between links  $i$  and  $j$ . (b) For two links  $i$  and  $j$  incident on two different receivers  $R_1$  and  $R_2$ :  $\bar{d}_{ij}(r) = d_{ij'}(r) + \bar{d}_{R_1, R_2}$ , where  $\bar{d}_{ab}$  is the algebraic distance from link  $a$  to link  $b$ , and  $j'$  is parallel to link  $j$ , incident on receiver  $R_1$ . The distance  $D_{ij}$  [see Eq. (18)] is thus given by  $D_{ij}(\delta) = L \sin(\delta/2) \cos(\beta) + \bar{d}_{R_1, R_2}$ , such that the links can also be assimilated to their center points.

4DVAR algorithms. An accurate description of YAO can be found in Thiria et al. (2006) and Nardi et al. (2009), and on the LOCEAN website (<http://www.loecean-ipsl.upmc.fr/~yao/>). The aforementioned papers provide a complete description of this software and the implicit mathematical principles.

The cost function is minimized with M1QN3, an algorithm developed by the Institut National de Recherche en Informatique et en Automatique (INRIA), which uses a quasi-Newton technique to solve unconstrained optimization problems. This algorithm is presented in Gilbert and Lemaréchal (2006) and is interfaced with the YAO software.

#### 4. Determining the advection velocity

In this section, we present the technique used to produce simulated data. We then describe the triangulation algorithm used to determine the advection velocity. Finally, we evaluate the performance of this algorithm using the simulated data.

##### a. Generation of simulated data

The aim of this method is to use 2D rainfall maps to produce Ku attenuation time series along the links. Simulated rainfall fields are generated by a 2D multifractal model [developed by Lovejoy and Schertzer (1990), using the rain parameters determined by Verrier et al. (2010)] that is able to reproduce the natural spatial variability of rainfall. In each simulation, the maximum rainfall rate is set to  $100 \text{ mm h}^{-1}$  and the rain percentage is set to 60%. Then, for a given (homogeneous and constant, as described in section 3a) advection velocity, the rainfall field is propagated through time at this velocity using the numerical method described in section 3a.

During this advection phase, the attenuations produced by the field along the paths of the microwave links are determined using Eq. (1).

##### b. Advection velocity estimation

The aim is to estimate the advection velocity of the attenuation fields, using the recorded satellite link measurements. Zinevich et al. (2009) estimated such a velocity. But because their measuring device consists of a large number of microwave links, they were able to use a method developed in Desa and Niemczynowicz (1997). In the present study we present a new triangulation method, adapted to the case of a network of sparse microwave links with a specific anisotropic geometry. This approach involves the numerical minimization of a cost function  $J_1$ :

$$J_1(\delta, \mathbf{V}) = \frac{\|\mathbf{D}(\delta) - \mathbf{V}\boldsymbol{\tau}\|^2}{\|\mathbf{D}(\delta)\|^2}, \quad (14)$$

where  $\delta$  is the direction (azimuth) and  $\mathbf{V}$  is the velocity of the advection (see Fig. 4). Vector  $\mathbf{D}(\delta)$  comprises the distances between each pair of satellite links (see below) and  $\boldsymbol{\tau}$  is the vector comprising the experimental time lags between the arrival of rainfall events at each pair of links. The latter terms are calculated using the method presented in the next section.

##### 1) TIME LAGS

Let  $\mathbf{A}_1, \dots, \mathbf{A}_p$  be the integrated rain attenuation vectors measured along  $p$  satellite-to-Earth microwave links during a rain event and let  $N$  be the number of measurements available for this event (and thus the size of vectors  $\mathbf{A}_i$ ). The cross-correlation function between links  $i$  and  $j$  is then defined as

$$\forall m \in [[-N; N]]:$$

$$C_{ij}(m) = \begin{cases} \sum_{k=1}^{N-m} \mathbf{A}_i(k+m) \mathbf{A}_j(k) & \text{if } m > 0 \\ C_{ji}(-m) & \text{if } m < 0. \end{cases} \quad (15)$$

It is assumed that for each value of the pair  $(i, j)$ , the value  $\tau_{ij}$  that maximizes the cross-correlation function corresponds to the time lag between time series  $i$  and  $j$ , whereas the corresponding value of the cross-correlation function  $\widetilde{C}_{ij} = C_{ij}(\tau_{ij})$  indicates the strength of the correlation between the two series.

## 2) DISTANCES

The distances  $\mathbf{D}(\delta)$  between the satellite links defined by Eq. (14) depend on the advection direction. In this section, we define  $\mathbf{D}(\delta)$  and show that the distance between the Ku links is the distance between their centers.

It is assumed that the rain front is perpendicular to the wind direction (characterized by the angle  $\delta$ ; see Fig. 4) and is moving in this direction. If  $d_{ij}(r)$  is the distance between the two parallels to the rain front passing through the points  $P_i$  and  $P_j$ , located on the links  $i$  and  $j$  at a distance  $r$  from the receiver, as shown in Fig. 4a, then the mean distance between links  $i$  and  $j$  is given by

$$D_{ij} = \frac{1}{L} \int_0^L d_{ij}(r) dr, \quad (16)$$

where  $L$  is the pathlength. Note that here, the lengths of the links are assumed to be equal. But we could show that the results of this section are still verified in the case of links of unequal length.

The following expression is derived for the function  $d_{ij}$ :

$$d_{ij}(r) = 2r \sin\left(\frac{\beta}{2}\right) \cos(\delta), \quad (17)$$

where  $\beta$  is the angle between links  $i$  and  $j$ .

This leads to the following expression for the distance  $D_{ij}$ :

$$D_{ij}(\beta) = L \sin\left(\frac{\beta}{2}\right) \cos(\delta). \quad (18)$$

Finally, from Eq. (18) it follows that the links can be assimilated to their center points [because  $D_{ij}(\beta) = d_{ij}(L/2)$ ].

In the above-mentioned calculations, it is assumed that just one receiver monitors all of the  $p$  satellite links. However, the final result of this section (that the links can be assimilated to their center points) remains valid when determining the distance between two links

monitored by two different receivers. Further details of this result are provided in Fig. 4b.

## c. Results

When only one receiver is used, the preceding result leads to nonunicity of the solution, since the center points of the links are almost aligned. In such a case, the pair  $(\delta_m, V_m)$  minimizing the cost function  $J_1$  defined by Eq. (14) is not unique. For each value  $\widehat{\delta}$  of wind direction, there is a corresponding wind speed  $V(\widehat{\delta})$ , which satisfies  $J_1[\widehat{\delta}, V(\widehat{\delta})] = \min_{\delta, V} [J_1(\delta, V)]$ . Under these conditions, only the wind speed can be deduced from the wind direction, or vice versa. Figure 5a illustrates this case with a simulated example (further details concerning the link's characteristics are provided in the caption). This difficulty can be avoided by adding a second receiver: under these conditions, there is only one pair of wind parameters  $(\delta_m, V_m)$  that can minimize the cost function of Eq. (14). This result is illustrated in Fig. 5b.

Note that when using simulated data, the results can be improved by positioning the second receiver as far as possible from the first receiver (provided both receivers are simultaneously affected by the same rain cells). However, when running the assimilation algorithm, it is preferable for the second receiver to be positioned relatively close to the first. A compromise separation of approximately 2.5 km was found to provide satisfactory results.

## d. Method used for observations with a single sensor

The experiments on real data presented in section 6 of this paper were recorded with just one receiver that was able to simultaneously monitor the signals emitted by four satellites. This configuration led to the measurement of four distinct Earth-satellite links. Under these conditions, as described above, the advection parameters cannot be directly estimated from the attenuation measurements. A different approach was thus used in order to determine these parameters from the radar data (see section 2): this involved calculating the distance and direction leading to the strongest correlation between successive radar maps. This method allows the distance between the two maps to be retrieved, from which the associated velocity vector can be determined.

## 5. Results based on simulated data

In this section, we evaluate our reconstruction method with simulated data. Section 5a describes the features of the simulated Ku links. In section 5b, we define the validation areas. Section 5c provides a statistical evaluation of the model's performance in the absence of

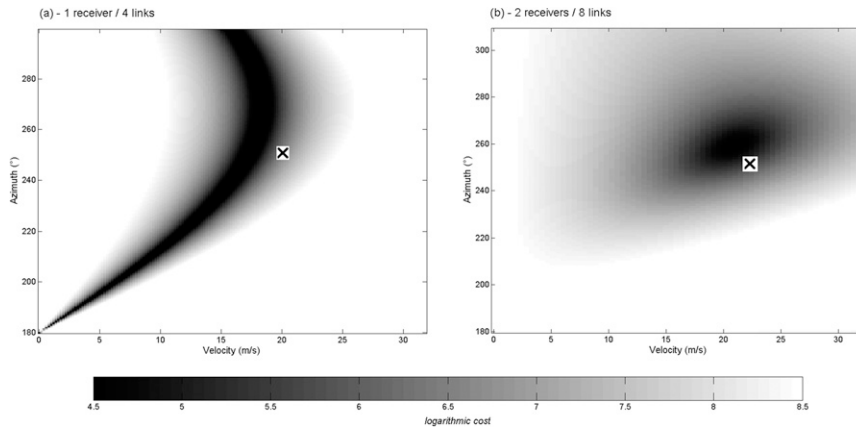


FIG. 5. Values of the cost function defined by Eq. (14) for simulated attenuation data with a wind velocity  $V = 20 \text{ m s}^{-1}$  and azimuth  $\delta = 250^\circ$  (real values indicated by a black cross). The simulated measuring device comprises (a) one receiver receiving four satellite-to-Earth microwave links and angularly separated from one another by  $20^\circ$  and (b) two receivers of the same type, separated by 2.15 km. Whereas the first system does not allow both advection speed and azimuth to be rebuilt (1D cost function minimum), the second system allows a relatively accurate solution to be found: the rebuilt advection is  $21 \text{ m s}^{-1}$  and  $259^\circ$ . Section 4a provides a description of the method used to generate simulated data.

perturbations, together with some results. We comment on the influence of the geometry of the simulated context on these results. Finally, in section 5d, we provide a qualitative evaluation of our algorithm's response when errors are added to the link pathlengths and advection velocity estimations.

#### a. Link characteristics

The method used to produce simulated attenuation time series is described in section 4a. Here, we simply add white noise to these attenuation time series. The noise has a uniform distribution centered around 0 and a width of 0.5 dB, corresponding to the uncertainty typically associated with satellite microwave attenuation measurements (Barthès and Mallet 2013). The resulting attenuation time series were used as input data for the assimilation algorithm.

We simulate the use of either one or two Ku sensors, with each of these receiving microwave signals from four different satellites. For each sensor, the azimuths of the four satellite links are  $150^\circ$ ,  $170^\circ$ ,  $190^\circ$ , and  $210^\circ$  (with  $180^\circ$  corresponding to the north/south axis). All eight links have the same length, equal to 7 km. The second sensor is located 2 km east and 0.8 km south of the first sensor, thus at a distance of 2.2 km compatible with the estimated optimal distance (2.5 km; see section 4c).

#### b. Evaluation area (assimilation area)

As described above, the algorithm produces rain fields over a rectangular  $N \times N$  grid [covering an area of  $(N\Delta x)^2 \text{ km}^2$ ]. However, the algorithm is not able to

rebuild realistic fields over the full grid. Although some portions of the rain fields are positioned on the grid, they never pass above the Ku links and are thus never recorded. For the purposes of evaluating the algorithm's performance, we thus reduce the grid to a "large assimilation area," defined as the area "seen" by the Ku links, as shown in Fig. 6. For a total simulation time of  $T$  seconds and a rainfall map considered  $t$  seconds after the beginning of the simulation, our large assimilation area is defined as that portion of the rain field that will pass through the links before the end of the simulation [rectangle of length  $\mathbf{V}(T-t)$ , where  $\mathbf{V}$  is the advection velocity; see Fig. 6].

We also introduce a "small assimilation area," defined as the area directly below the Ku links (see Fig. 6). This second area is introduced for two main reasons. First, the large assimilation area is not fixed, since it depends on the advection speed and direction, and on the simulation time. The small assimilation area has a fixed position. Second, in the present section (simulated data), the model is assumed to be perfect. However, in real situations the model can be affected by large errors (for instance, numerical diffusion, or nonadvective events; see section 6). The small assimilation area thus allows the algorithm to be evaluated over a more constrained area, situated just below the links.

In the present section, all of the figures and statistics are restricted to the large assimilation area.

#### c. Statistical results

Fifteen initial rainfall fields were produced by the multifractal model, with a spatial resolution of  $0.4 \text{ km} \times 0.4 \text{ km}$

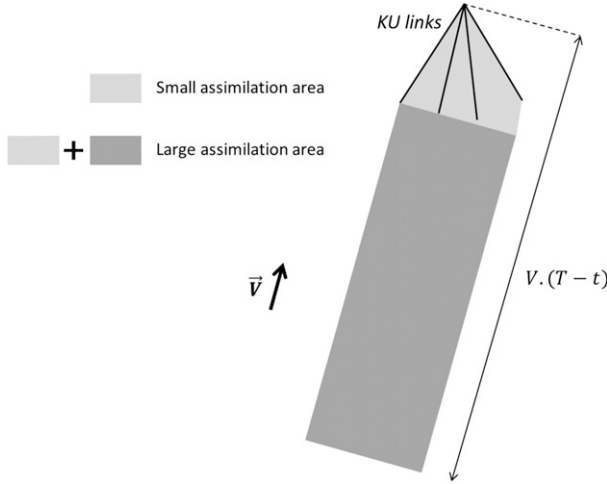


FIG. 6. Small and large assimilation areas as defined in section 5b. The advection velocity is represented by  $\mathbf{V}$ ,  $T$  is the total simulation time, and  $t$  is the time of the rain field under consideration.

on a  $68 \times 68$  grid, so that the total area covered was close to  $27 \text{ km} \times 27 \text{ km}$ . For each of these 15 fields, we then created the corresponding attenuation time series using the method described in section 4a, with an advection velocity chosen to ensure that the rainiest portion of the field passes above the microwave links during the advection phase (phase during which the attenuation time series are created). The velocities, which were chosen in order to limit the total duration of the simulations to approximately 30 min, thus ranged from 9 to  $21 \text{ m s}^{-1}$ . The advection azimuths ranged from  $180^\circ$  (south wind) to  $270^\circ$  (west wind). These characteristics are coherent with those encountered during all of the strong rain events monitored during our case studies.

Finally, the attenuation series are assimilated. The value of the cost function weighting coefficient  $c_f$  [Eq. (11)] was set to  $7 \times 10^{-3}$ . This value was chosen in order to ensure that, after a few iterations of the minimizer, the observation and filter components of the cost function would be nearly balanced. Otherwise, the minimizer would focus on minimizing the most strongly weighted component of the cost function, and the other component of this function would contribute nothing to the results. Note that the value assigned to this parameter depends on the weighting of the observation component of the cost function, and thus on the total quantity of rain falling above the microwave links during the experiment (in the case of a greater quantity of rain, the attenuation is stronger, a higher number of observations is available, and the observation component of the cost function has a higher weight). In these simulated experiments, the total rainfall remains almost constant (all of the initial fields are generated with a multifractal model using the same

parameters), such that the value of  $c_f$  does not change. With real data, the total rainfall above the links can vary strongly from one event to another. In such a case, an initial weighting coefficient is selected and the cost function is evaluated after a small number of iterations of the minimizer. The weighting coefficient is then adjusted so that the two components of the cost function are balanced. This method could probably be improved, for example, by automatically adjusting  $c_f$  during the minimization process.

We define the following indicators to quantify the method's performance. The first of these is the absolute bias  $b_a^n$  defined by

$$b_a^n = |m_n^{\text{as}} - m_n^0|, \quad (19)$$

where  $m_n^{\text{as}}$  and  $m_n^0$  indicate the mean rainfall rates of the assimilated and original initial fields, respectively, for the  $n$ th experiment (with  $n$  ranging from 1 to 15).

Using the same notations, the relative bias  $b_r^n$  can be defined as a percentage by

$$b_r^n = 100 \left( \frac{m_n^{\text{as}} - m_n^0}{m_n^0} \right). \quad (20)$$

To evaluate the model's ability to reproduce the strongest parts of the rain cells, we also calculate the mean bias at the 95% percentile, defined as

$$b_{95\%} = \frac{1}{15} \sum_{n=1}^{15} (m_{95,n}^{\text{as}} - m_{95,n}^0), \quad (21)$$

where  $m_{95,n}^{\text{as}}$  and  $m_{95,n}^0$  indicate the value of the 95% percentile of the field for the  $n$ th experiment for the assimilated and original fields, respectively.

Finally, the root-mean-square error  $\text{rmse}^n$  is defined as

$$\text{rmse}^n = \sqrt{\frac{1}{N} \sum_{(S)} [(R_n^{\text{as}})_{ij} - (R_n^0)_{ij}]^2}, \quad (22)$$

where  $(R_n^{\text{as}})_{ij}$  and  $(R_n^0)_{ij}$  are the assimilated and original initial rainfall fields of the  $n$ th experiment at grid point  $(i, j)$ , respectively, where  $(S)$  is the large assimilation area and  $N$  is the number of grid points in the  $(S)$  area.

Table 2 provides a summary of all these indicators, in terms of bias and standard deviation over the 15 simulations, when one or two Ku sensors are available.

Table 2 shows that the assimilation algorithm accurately reproduces the total rainfall rate over the area, with a mean absolute bias of only 2.0% associated with the use of eight microwave links. Moreover, the algorithm does not produce any significant systematic

TABLE 2. Statistical results on 15 simulated assimilation experiments: mean and standard deviation of the absolute bias  $b_a^u$  [Eq. (19)], mean of the absolute relative bias  $|b_r^u|$  [see Eq. (20)], mean relative bias  $b_r^u$  [Eq. (20)], mean bias to the 95% quantile  $b_{95\%}$  [Eq. (21)], and mean and standard deviation of the root-mean-square error  $\text{rmse}^u$  [Eq. (22)].

		2 Ku sensors ( $2 \times 4$ microwave links)	1 Ku sensor (4 microwave links)
Absolute bias ( $\text{mm h}^{-1}$ )	Mean	0.8	2.1
	Std dev	0.5	1.8
Absolute relative bias	Mean	2.0%	5.2%
Relative bias	Mean	+0.3%	+3.6%
$b_{95\%}$ ( $\text{mm h}^{-1}$ )		+4.0	+11.1
RMSE ( $\text{mm h}^{-1}$ )	Mean	12.4	21.6
	Std dev	6.3	6.6
Mean rainfall rate ( $\text{mm h}^{-1}$ )			40

deviation since the relative bias over the 15 simulations is only +0.3%. The absolute bias is very small ( $0.8 \text{ mm h}^{-1}$ ) compared to the mean rainfall rate in the assimilation area, which is approximately  $40 \text{ mm h}^{-1}$  (ranging from  $27.6$  to  $48.4 \text{ mm h}^{-1}$ ). The standard deviation for the combined 15 simulations is equal to  $0.5 \text{ mm h}^{-1}$ , which thus indicates that the algorithm accurately reproduces the total rain. When only one receiver is used (corresponding to just four satellite-to-Earth microwave links), there is an associated decrease in the quality of the results (mean absolute error =  $2.1 \text{ mm h}^{-1}$  with a standard deviation of  $1.8 \text{ mm h}^{-1}$  and a mean overestimation of the rainfall of 3.6%). These results remain satisfactory and do not show any reason to not support the use of this algorithm in the current experiment with only one receiver (see section 6).

Finally, a pixel-to-pixel comparison reveals a mean RMSE of  $12.4 \text{ mm h}^{-1}$  with a standard deviation of  $6.3 \text{ mm h}^{-1}$ . This value is quite satisfactory (the average rain rate is close to  $40 \text{ mm h}^{-1}$ ), but it must be used with care: when working with real data, many sources of error are introduced such that these point-to-point comparisons will no longer be realistic. Nevertheless, these results show that the use of only one receiver does not strongly disturb the model, since it finds a mean RMSE of  $21.6 \text{ mm h}^{-1}$  and a similar standard deviation.

One notable geometric characteristic of the microwave links used in this study is their anisotropy. As these links are directed mainly southward from the sensor (since they correspond to geostationary satellites observed from the Northern Hemisphere), it is reasonable to expect the results to be better with westerly winds than with southerly winds. In the first case, the links will be successively traversed by the rain front, whereas in the second case they will be traversed simultaneously. Moreover, in the first case, each portion of the rain cell will necessarily advance successively through each of the links. On the other hand, if the rain field is advected northward, then some portions of the rain cells may

advance between two links without touching either of these for a significant length of time, thus making the minimization and determination of field features more difficult.

Our simulations confirm this assumption. We recalculate the statistics of Table 2, while distinguishing the events arriving mainly from south (meaning, with an advection azimuth between  $180^\circ$  and  $225^\circ$ ) from the events arriving mainly from west (advection azimuth between  $225^\circ$  and  $270^\circ$ ). We note that from a total of 15 simulations, 8 had a northward velocity and 7 had an eastward velocity. In the case of the northward events, the mean absolute bias is  $1.0 \text{ mm h}^{-1}$  (2.5%) and the root-mean-square error is  $15.7 \text{ mm h}^{-1}$ , whereas these values are  $0.6 \text{ mm h}^{-1}$  (1.4%) and  $8.7 \text{ mm h}^{-1}$ , respectively, for the eastward events. This confirms the expected outcome of mainly west/east advected events being easier to rebuild with our algorithm than the north/south advected events.

We also note (Table 2) that the model overestimates the 95% quantile by  $4 \text{ mm h}^{-1}$  (note that the mean value of the 95% quantile over the 15 simulations is approximately  $73 \text{ mm h}^{-1}$ ). Although this overestimation is quite small, it is significant, especially as all of the simulations overestimate the value of the 95% quantile. This outcome is probably due to the propagation model used and its associated numerical diffusion. Very strong, localized gradients on the initial field are very quickly smoothed by the numerical model during advection, meaning that they do not significantly increase the cost function, even with a strong filter term [see section 3b(2)]. However, by placing very high rainfall rates on the borders of the assimilation area, the algorithm gains new degrees of freedom. These high rainfall rates, which occur during the advection phase, are also numerically smoothed, thereby helping the algorithm to adjust the cost function, even at the center of the assimilation area. This phenomenon occurs mainly with rainfall events accompanied by a southerly wind, during which it is

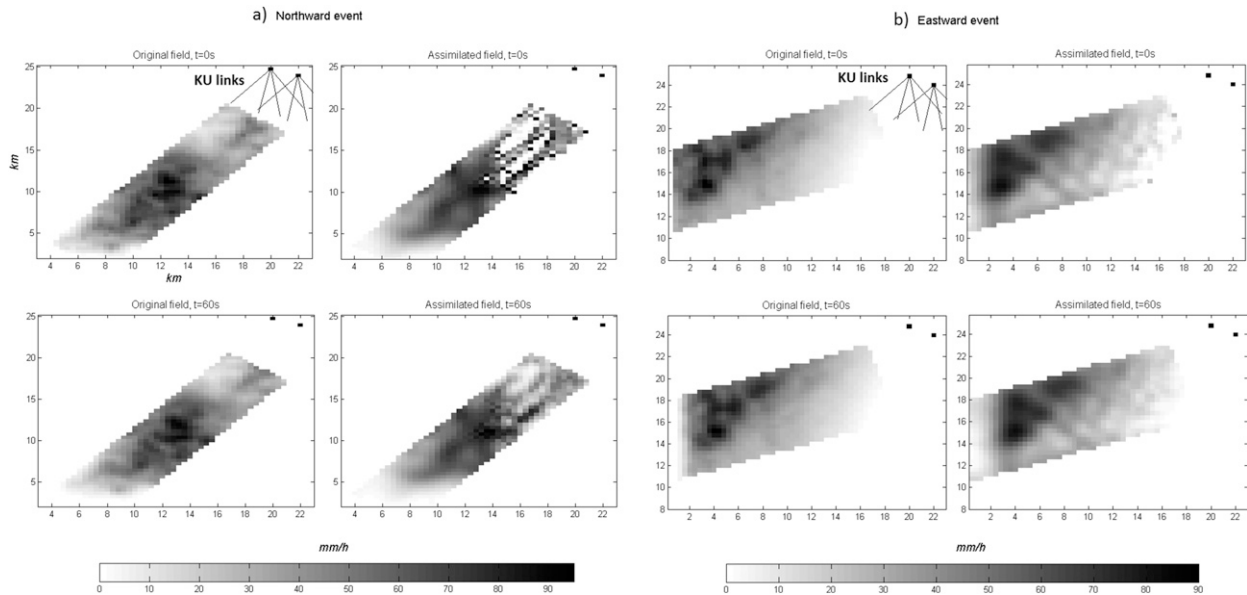


FIG. 7. Results of two assimilation experiments run with simulated data (recorded by two Ku receivers), using different original rain fields and advection parameters. (a) Results for a mainly northward event. The advection azimuth is  $217^\circ$  and the advection speed is  $17.1 \text{ m s}^{-1}$ . (left column) The original field (to be rebuilt) at  $t = 0$  (initial field, top row) and after 60 s (advected by the numerical scheme, bottom row). (right) The rain field rebuilt by the assimilation algorithm at  $t = 0$  and after 60 s. (b) As in (a), but for a mainly eastward event. The advection azimuth is  $253^\circ$  and the advection speed is  $17.9 \text{ m s}^{-1}$ .

more difficult for the microwave link geometry to accurately locate the rain cells. Figure 7 provides a good illustration of this phenomenon. Figure 7a shows the results of an assimilation experiment for a mainly southerly event. The upper part of the figure compares the original field with the rebuilt field at  $t = 0$ . Although the total rainfall over the area is reproduced with reasonable accuracy, the assimilated field has a significant number of very steep gradients, with some pixels having rainfall rates more than  $90 \text{ mm h}^{-1}$  in excess of that of dry neighboring pixels. The lower part of the figure represents the same fields, 1 min later. The steep gradients of the assimilated field have been strongly smoothed, so that the error produced by these gradients does not have a strong influence on the cost function. This phenomenon is not observed in the case of events accompanied by a westerly (Fig. 7b), because each rain cell passes successively through the path of each microwave link. This phenomenon could be reduced by carefully adjusting the weighting of the filter term for each simulation, or by adding various constraints at the level of the cost function to the rain field's characteristics (and replacing the filter by these constraints). We also note that decreasing the spatial resolution of the rebuilt fields (e.g., by averaging these fields on a  $1 \text{ km} \times 1 \text{ km}$  grid) smooths the fields and reduces the extent of this problem. As already described, this phenomenon is amplified by the use of a single receiver, which leads

to a small overestimation of the 95% quantile (mean excess of  $11.1 \text{ mm h}^{-1}$ ), which nevertheless remains reasonable.

These statistical results show that the algorithm is efficient for the processing of simulated data with no error model. Overall, the rain field features are satisfactorily reproduced (no systematic under- or overestimation of the total rainfall, a small mean absolute bias, and point-to-point errors that are small in comparison with the rain rates). It is also shown that, although the results are deteriorated by the use of only one receiver, they remain acceptable. Nevertheless, these results show that our model could be applied to real data. But under these conditions, various sources of error can be expected to affect the estimations.

#### d. Impact of uncertainties of link length and advection parameters

In this section, the algorithmic parameters, such as the advection velocity vector or the length of the Ku links, are called input parameters. In a case study with real data, these parameters are evaluated with a certain degree of uncertainty. The aim of this section is to qualitatively assess the algorithm's response when these parameters are not accurately known. Only qualitative results are given here: during real measurements, larger errors can be expected as a consequence of inaccuracies in the model itself (real events are not purely advective;

TABLE 3. Mean ( $\rho$ ) and standard deviation ( $\sigma$ ) of the normalized maximum value of cross correlations between successive radar maps, for eight rain events observed in 2013. Advection parameters determined from the analysis of radar maps. Mean and maximum attenuations recorded by the Ku sensor during the rain events. Estimated freezing level, derived from the temperature at the Aubenas Météo-France weather station.

No.	Date	Beginning time (UTC)	End time (UTC)	$\rho$	$\sigma$	Advection		Attenuation (dB)		Freezing level
						Velocity ( $\text{m s}^{-1}$ )	Direction ( $^{\circ}$ )	Mean	Max	
1	7 Sep	1400	1435	0.90	0.025	11.5	210	1.64	5.29	3.5 km
2	7 Sep	1735	1810	0.81	0.026	12.6	199	1.19	5.00	3.0 km
3	8 Sep	1440	1525	0.81	0.082	6.2	238	2.51	12.78	3.9 km
4	28 Sep	1805	1840	0.90	0.015	13.6	191	1.20	9.89	3.5 km
5	29 Sep	0205	0250	0.89	0.019	7.9	208	4.37	13.97	2.8 km
6	4 Oct	1745	1825	0.81	0.030	12.1	194	1.95	7.49	3.0 km
7	20 Oct	0635	0705	0.92	0.018	16.2	220	2.56	11.28	2.5 km
8	20 Oct	0820	0850	0.89	0.015	16.2	220	5.32	12.48	2.5 km

see below). Furthermore, the statistical results corresponding to simulated idealized cases would not be representative of the results obtained during a real rainfall scenario.

We first studied the influence of an error on the length of the links. For this, the observations (i.e., attenuations) were initially simulated with the lengths of the Ku links set to  $L = 7$  km. During the assimilation process, the parameter  $L$  was then decreased to 6.5 km, leading to an overestimation of the rainfall in the southern portions of the links: the algorithm assigns the same volume of rain to a smaller area (since the assimilation area is reduced when the length of its associated link is decreased). The algorithm allocates the rain “excess,” recorded by those portions of the links that have been removed, to the southern portion of the new shortened links. However, the total rain mass is correctly reproduced. We also studied the influence of an error in advection speed. Simulations show that a decrease in advection speed acts like a contraction operator on the resulting field, in addition to shifting it toward the location of the microwave links, whereas an increase in advection speed produces the opposite effects. This outcome can be explained by the fact that when the advection speed is decreased, the resulting rainfall field has to be shifted closer to the microwave links (in order to transit above them at the correct time) and must be compressed in order to take the same time to pass over the links. Once again, the total rain mass is well reproduced.

## 6. Results with experimental data

In this section, we present the rainfall events monitored in 2013 with the measuring device described in section 2. This is followed by a discussion of the results.

### a. Description of the events

Eight rain events were observed with the Ku links during the autumn of 2013. Table 3 presents the main features of these events. They were generally quite intense (the maximum attenuation is always greater than 5 dB) and moved mainly northward (mean advection direction of  $210^{\circ}$ ). The mean attenuation rates along the microwave links ranged between 1.20 and 5.3 dB. Events longer than 45 min were split into separate independent components.

As described in section 3b, our 4DVAR algorithm is designed to rebuild the initial ( $t_0$ ) attenuation field, so that the differences between the latter field (when it is propagated through time by the numerical model) and the observations are minimized. In section 3a the numerical model used in this study is shown to be purely advective. This assumption is clearly a broad simplification that is not always verified, especially in a mountainous area such as the Cévennes–Vivarais region (Molinié et al. 2012). The upper part of Fig. 8 shows radar maps corresponding to an event that occurred on 8 September 2013 in the vicinity of the Ku links. Propagation of the rainfall cells during this event is clearly not advective, to the extent that the total rain over the area increases significantly during the event, due to orographic precipitation caused by vertical ascent of the air mass. Conversely, the lower part of Fig. 8 shows an event that occurred on 20 October 2013, during which the total rain rate appears to be quite well conserved and the propagation is relatively advective.

To evaluate the advective characteristic of the events, we introduce a statistical criterion that is the value of the maximum cross correlation between successive weather radar recordings. Table 3 presents, for our eight events, the mean and standard deviation of the normalized maximum cross correlations between all of the

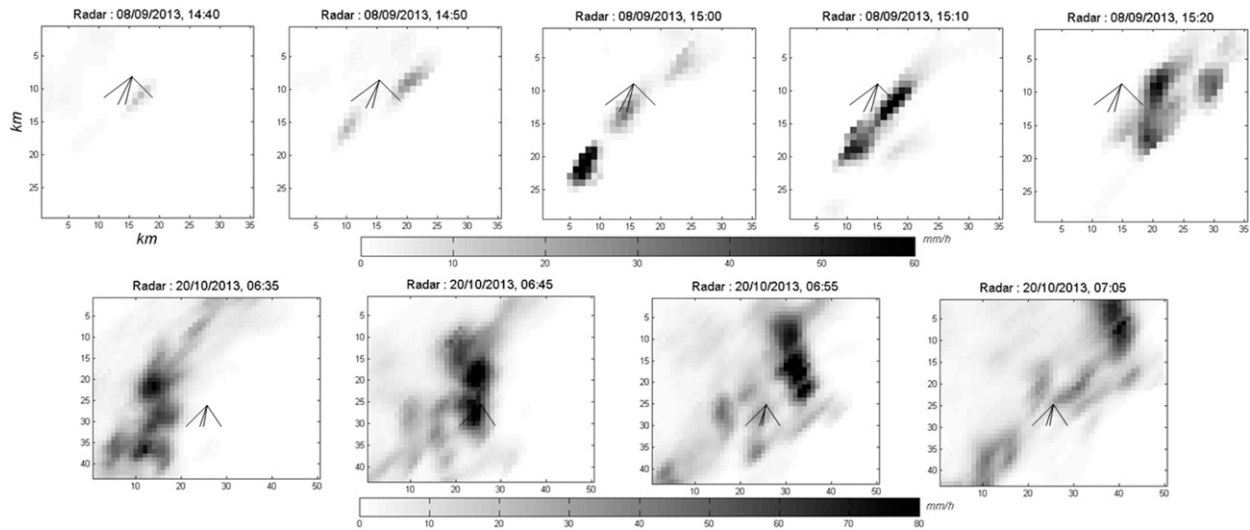


FIG. 8. Weather radar images around the Ku sensor, for two events recorded in 2013: (top) on 8 Sep and (bottom) on 20 Oct. The time lag between successive snapshots is 10 min. The four Ku links are represented by the continuous black lines.

successive 5-min radar maps. As it is reasonable to assume that the events with a large mean value and a small standard deviation are more “advective,” better results can be expected from our rebuilding algorithm when these events are analyzed. We thus selected four advective events (events 4, 5, 7, and 8).

### b. Results

In this section, Table 4 presents the results of numerical comparisons between Ku and radar rainfall fields for the eight aforementioned events and for the small and large assimilation areas (see section 5b) at

TABLE 4. Correlation coefficients  $r$  between radar and Ku-band (microwave) rain fields; regression line equations for two different spatial resolutions; bias (corresponding to the difference between the mean values of microwave and radar rainfall measurements); average radar rain rates; and relative bias (sixth column divided by seventh column) for the eight events studied in 2013. These statistics have been computed for both the small and large assimilation areas defined in section 5b.

Small assimilation area							
Event (see Table 3)	$r$		Regression line		Bias ( $\text{mm h}^{-1}$ )	Avg rain rate ( $\text{mm h}^{-1}$ )	Relative bias (%)
	$1 \text{ km} \times 1 \text{ km}$	$2 \text{ km} \times 2 \text{ km}$	$1 \text{ km} \times 1 \text{ km}$	$2 \text{ km} \times 2 \text{ km}$			
4 (28 Sep)	0.85	0.92	$0.98x + 1.3$	$1.08x + 0.5$	+1.1	5.2	+21
5 (2 Sep)	0.77	0.84	$0.95x + 0.5$	$0.94x + 1.1$	-0.7	24.9	-2.8
7 (20 Oct)	0.81	0.88	$0.44x + 6.1$	$0.55x + 2.5$	-7.9	25.1	-31
8 (20 Oct)	0.39	0.82	$0.40x + 26$	$0.83x + 3.5$	-2.7	47.1	-5.7
1 (7 Sep)	0.69	0.67	$0.19x + 4.4$	$0.24x + 2.6$	-12.8	21.3	-60
2 (7 Sep)	0.17	0.32	$0.13x + 0.3$	$0.19x + 1.5$	-5.5	9.0	-61
3 (8 Sep)	0.62	0.66	$0.47x + 9.9$	$0.54x + 6.9$	+2.7	13.8	+20
6 (4 Oct)	0.42	0.63	$0.36x + 8.9$	$0.54x + 4.8$	-0.3	14.4	-2.1
Large assimilation area							
Event (see Table 3)	$r$		Regression line		Bias ( $\text{mm h}^{-1}$ )	Avg rain rate ( $\text{mm h}^{-1}$ )	Relative bias (%)
	$1 \text{ km} \times 1 \text{ km}$	$2 \text{ km} \times 2 \text{ km}$	$1 \text{ km} \times 1 \text{ km}$	$2 \text{ km} \times 2 \text{ km}$			
4 (28 Sep)	0.48	0.52	$0.68x + 1.3$	$0.74x + 0.97$	-0.1	3.6	-2.7
5 (29 Sep)	0.51	0.53	$0.53x + 3.8$	$0.51x + 4.7$	-6.9	34.7	-20
7 (20 Oct)	0.81	0.87	$0.58x + 3.5$	$0.68x + 2.0$	-2.1	12.2	-17
8 (20 Oct)	0.64	0.78	$0.72x + 4.7$	$0.85x + 1.3$	-6.5	35.4	-18
1 (7 Sep)	0.72	0.70	$0.21x + 2.0$	$0.23x + 1.3$	-10.8	16.0	-68
2 (7 Sep)	0.41	0.49	$0.26x + 0.34$	$0.30x + 0.14$	-6.6	9.0	-73
3 (8 Sep)	0.52	0.67	$0.45x + 14$	$0.61x + 8.1$	+3.5	19.5	+18
6 (4 Oct)	0.43	0.61	$0.33x + 5.6$	$0.45x + 3.5$	-7.9	19.9	-40

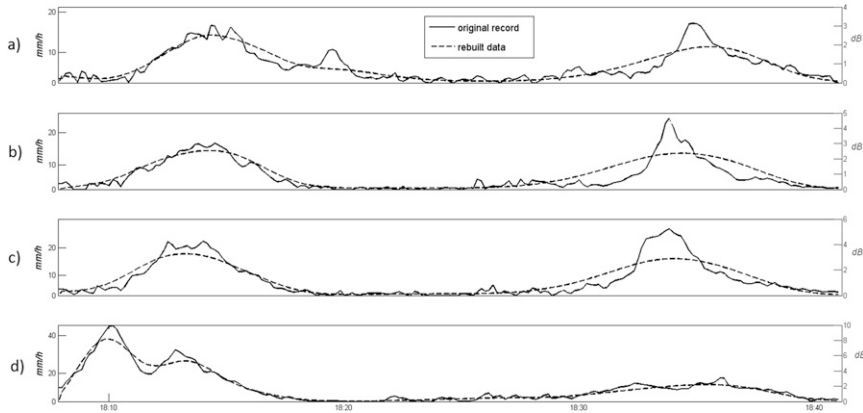


FIG. 9. Integrated rainfall along the four microwave links as recorded by the Ku sensor (solid lines) and reproduced by the assimilation algorithm (dashed lines), during the event that occurred from 1810 to 1840 UTC on 28 Sep 2013. Plots (a)–(d) represent data from the most westward link to data from the most eastward link (see Fig. 2).

different spatial resolutions. Figure 9 reveals the algorithm’s ability to reproduce the observations above the Ku links. For the case of the rain event that occurred on 28 September, Fig. 10 provides a comparison between

the Ku and radar fields. Figure 11 presents the boxplots of the “error” (i.e., the difference between the radar and Ku rainfall fields) for 1 and 4 km<sup>2</sup> rainfall fields. Figure 12 presents the cumulative rainfall recorded by

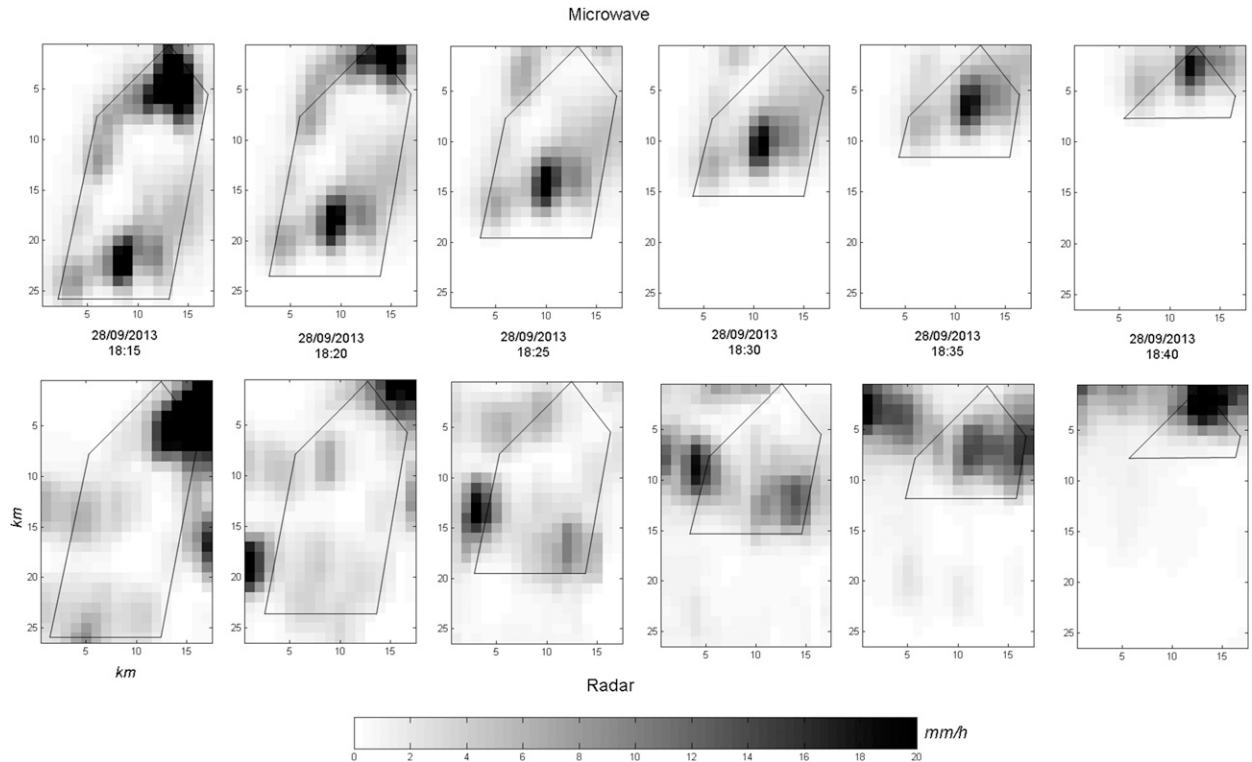


FIG. 10. (top) The 5-min integrated rain fields, rebuilt every 5 min by the assimilation algorithm, using Ku data recorded during the rainfall event of 28 Sep 2013. Following the hypothesis made in this study, the initially rebuilt field (at 1815 UTC, in the top left-hand corner) is advected at the next time steps only, which means that the rain cell passing over the Ku links at 1835 UTC was positioned to the southwest of the links at 1815 UTC. (bottom) Images of the same rainfall fields, when observed by the Bollène weather radar. The area delineated in red is the large assimilation area defined in section 5b. The small assimilation area is indicated by a triangle situated above the large area (below the Ku links).

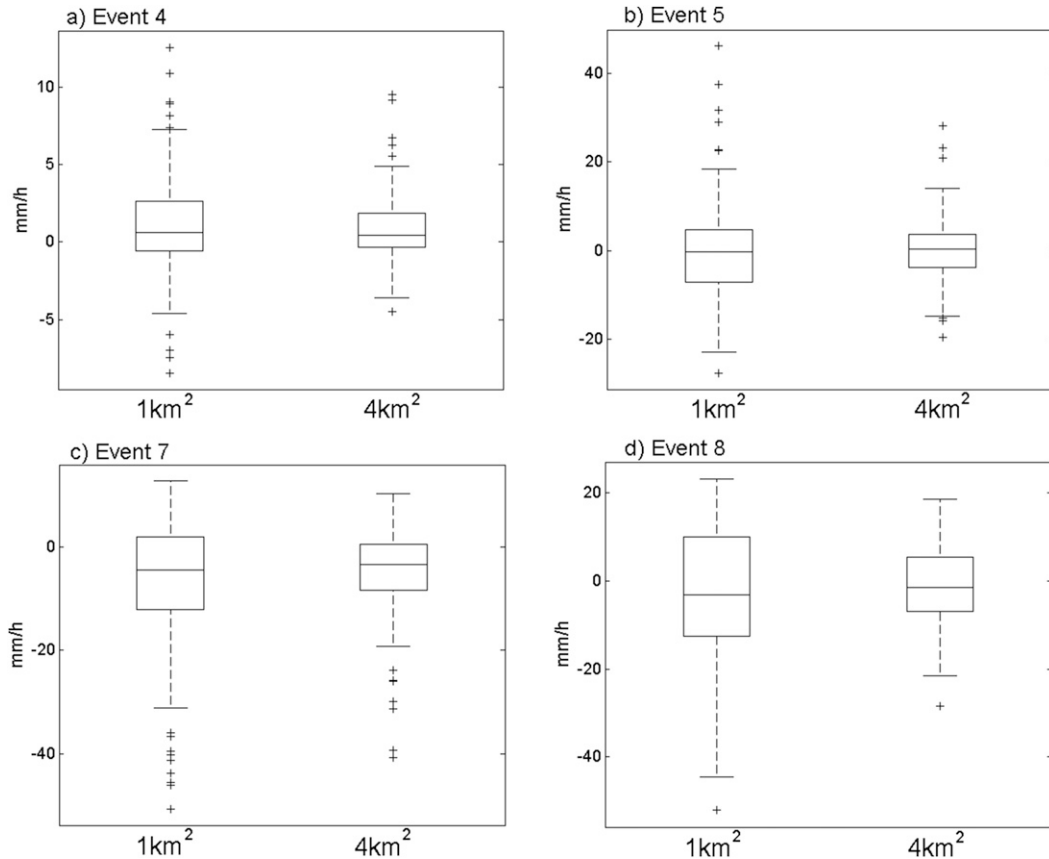


FIG. 11. Boxplots of the differences between radar and Ku rainfall rates in the assimilation area for the four studied advective events: (a) event 4, 28 Sep; (b) event 5, 29 Sep; (c) event 7, 20 Oct; (d) event 8, 20 Oct. For all of these events, we present the quantiles of the pixel-to-pixel differences on (left) a  $1 \text{ km} \times 1 \text{ km}$  grid and (right) a  $2 \text{ km} \times 2 \text{ km}$  grid.

the rain gauge at Mirabel, and the values of rainfall recorded by the radar and reproduced by the assimilation algorithm at the same location. The last two figures are restricted to the four advective events. Finally, Table 5 presents the correlation coefficients and regression line equations of Ku observations versus rain gauge data and radar measurements versus rain gauge data for various integration times ranging between 5 and 25 min.

### 1) RADAR COMPARISON

The Ku rainfall fields are first integrated in space and time, so that they have the same resolution as the radar data (i.e., 5 min in time and  $1 \text{ km}^2$  in space). In this section, we first perform numerical comparisons between radar and Ku fields and confirm the assumption that four of the eight events could not be correctly represented by our advection model. In the following, only the four advective events will be described. We then focus on the case study of the event that occurred on 28 September 2013 to demonstrate the performance of the algorithm. Finally, more general conclusions are presented.

The main parameter (among those presented in Table 4) involved in the evaluation of the ability of our advection model to correctly represent the propagation of rain fields is the mean bias found in the large assimilation area. If the actual propagation is not advective, then there must be some “creation” or “destruction” of rainfall during the simulation. Thus, since the total rain is conserved by our model, large biases can be expected, especially in the areas not directly covered by the Ku links. In three events the biases are large: events 1 (−68%), 2 (−73%), and 6 (−40%). Also note that these three events show very flat regression lines (with slopes generally below 0.5). This means that the Ku fields are strongly smoothed out in comparison with the radar fields. Their associated regression coefficients are also rather small. The two latter remarks also apply to event 3. For instance, in the small assimilation area and over a  $2 \text{ km} \times 2 \text{ km}$  grid, only these four events (1, 2, 3, and 6) have regression coefficients of less than 0.7. On the contrary, the regression coefficients of the other events are above 0.8 (note that event 8 has a small regression

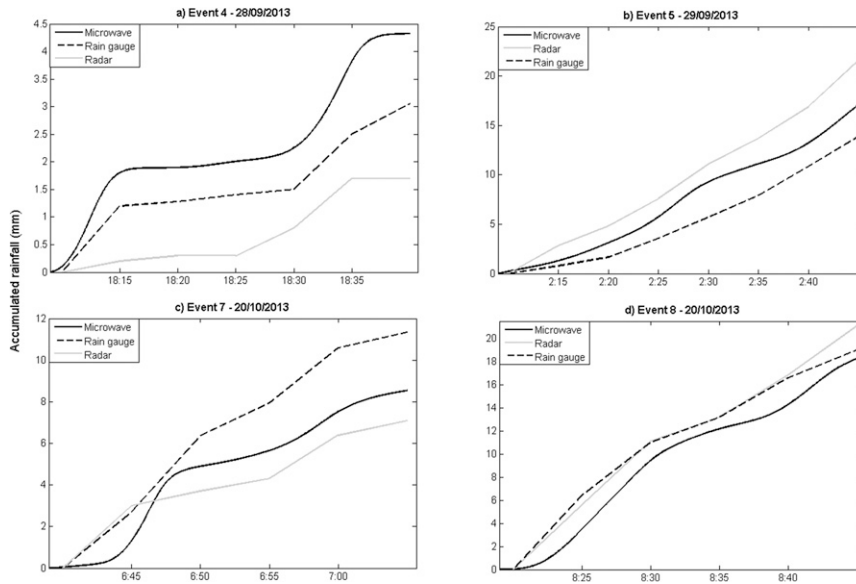


FIG. 12. Cumulative rainfall for the four rain events studied at Mirabel, Le Pradel ( $44^{\circ}58'N$ ,  $4^{\circ}50'E$ ; see Fig. 2). The data extracted from the  $500\text{ m} \times 500\text{ m}$  instantaneous fields, rebuilt by the assimilation algorithm (continuous black lines), are plotted against rain gauge data from Le Pradel (continuous gray lines) and data extracted from the  $1\text{ km} \times 1\text{ km}$  radar fields.

coefficient of  $0.39$  at  $1\text{ km}^2$ , but that this is no longer the case at  $4\text{ km}^2$ , suggesting a scaling problem, as explained below).

The statistical criteria defined for radar maps in the previous section will now be analyzed in more detail in order to detect the advective properties of events (see Table 3, columns 5 and 6). The four events for which poor results (1, 2, 3, and 6) were obtained are the only ones whose cross-correlation mean and standard deviation are less than  $0.85$  and greater than  $0.025$ , respectively. These events will be considered as nonadvective and will not be used again in the rest of this paper.

We will now focus on the 28 September event. As seen from the attenuation time series measured by the Ku sensor (see Fig. 9, solid lines) there are two distinct peaks along all of the four Ku links, with the first one occurring at approximately  $1810$  UTC and the second one at approximately  $1835$  UTC. The radar maps for this event (Fig. 10, bottom) show that the second peak corresponds to a rain cell that gradually intensified from  $1825$  to  $1840$  UTC as it moved northward while approaching the Ku sensor.

When looking at the results of the assimilation algorithm for this event, the following four main points can be noted:

TABLE 5. Point-scale rainfall estimations. Correlation coefficients, regression line equations at different time scales, and average biases between rain gauge and Ku data (third column) and between rain gauge and radar data (fourth column). Average rain rate recorded by the rain gauges. Four rain events and seven rain gauges are aggregated for these estimations (see section 6b).

	Time resolution (min)	Ku-rain gauges	Radar-rain gauges
$r$	5	0.63	0.69
	10	0.76	0.79
	15	0.77	0.83
	20	0.78	0.83
	25	0.82	0.84
Regression line equation	5	$0.53x + 0.64$	$0.61x + 0.64$
	10	$0.63x + 0.79$	$0.69x + 0.85$
	15	$0.62x + 1.08$	$0.69x + 1.16$
	20	$0.61x + 1.52$	$0.68x + 1.58$
	25	$0.57x + 1.58$	$0.64x + 1.56$
Bias ( $\text{mm h}^{-1}$ )		$-3.8$	$-1.9$
Rain gauges avg rain rate ( $\text{mm h}^{-1}$ )			24.5

- (i) The mean rainfall rate near to the microwave links (the small assimilation area) is suitably reproduced (with a mean bias of  $1.1 \text{ mm h}^{-1}$ ), as is the mean rainfall rate in the large assimilation area (with a bias of  $-0.1 \text{ mm h}^{-1}$ ). This shows once again that one advantage of this measuring device and reconstruction method is that all of the rain falling above the microwave links is seen (as a result of the very good temporal resolution of the device: 10 s). Thus, because of the space-integrated feature of the data and the assimilation algorithm, whose effect is to connect the measurements recorded at successive time steps, the total rain falling in the area of the satlinks during an event is well reproduced by the algorithm.
- (ii) The northern rain cell (corresponding to the first rainfall peak in Fig. 9) is correctly reproduced (see Fig. 10), while the southern cell is highly overestimated in the initial field (Fig. 10, left). This is a consequence of the model error. Pure advection is assumed by the propagation model, so that rain is perfectly conserved, whereas it has been seen above that the strength of the second rain cell increased while advancing. Consequently, the algorithm overestimates the initial rainfall so that, once advected above the microwave links, it provides realistic attenuation rates, albeit different from the actual ones. This model error can also be seen when comparing the radar/Ku correlation in the small assimilation area (0.85) with that obtained in the large assimilation area (only 0.48).
- (iii) The projection of the second rainfall peak on the Ku links is smoothed out by the assimilation algorithm (Fig. 9). This is another consequence of the model error. As seen before (section 5c), the model's numerical diffusion is significant, and therefore the strong rain gradients cannot be preserved through advection: the rebuilt time series are then smoothed in comparison with the original ones. However, it may be noted that this smoothing is rather small for this event, to the extent that it does not appear when performing a regression between rebuilt and radar rainfall fields (Table 4: the slope of the regression line is 0.98, which is very close to 1).
- (iv) The north/south variations of the rainfall fields seem to be better located and reproduced than the west/east variations (see Fig. 10). The event is mainly advected northward (azimuth:  $191^\circ$ ), so that the Ku links are almost perpendicular to the rain front direction. The rain front then gradually moves northward along the links, helping the algorithm to distinguish between the north/south rain variations. (For northward advection, the northern

part of the rain cell passes over the links before the southern part. For westward advection, both the northern and the southern parts of the rain cell pass simultaneously above the links.) However, it has already been pointed out above (section 5c) that this case (northward advection) is more difficult to solve numerically for the algorithm than is the other case (eastward advection). Additionally, all of the cases selected among the events shown in Table 3 are mainly advected northward.

The other events studied in this paper confirm the first point. The total rainfall is satisfactorily reproduced (Table 4; Fig. 11) both in the small and large assimilation areas.

The tendency of the algorithm to smooth the rain fields (point iii) is very clear for two events, namely, the fifth (29 September 2013) and the seventh (20 October 2013) events. This tendency appears both on the time series of rainfall above the microwave links and on the regression slopes between the radar and microwave fields (Table 4), with regression slopes of 0.44 and 0.40 at  $1 \text{ km}^2$  (small assimilation area), respectively.

The radar/microwave pixel-to-pixel ( $1 \text{ km}^2$ ) comparisons performed in the small area show a good agreement for three events (4, 5, 7, with correlation coefficients of 0.85, 0.77, and 0.81, respectively), but this is not the case for event 8, with  $r = 0.39$ , and a  $y$ -intercept value of  $26 \text{ mm h}^{-1}$ , which is excessively large. The latter failure also appears clearly from Fig. 11, which shows large values of the quartiles of the radar/microwave difference (around  $\pm 10 \text{ mm h}^{-1}$ ). However, when the resolution of the radar and microwave fields are reduced to a  $4 \text{ km}^2$  grid (Table 4; Fig. 11), the correlation coefficients significantly increase for all the events—to 0.92, 0.84, and 0.88 for events 4, 5, and 7, respectively, and from 0.39 to 0.82 for event 8—and the widths of the boxplots systematically decrease. This means that, even if the microwave field can be quite different from the radar field at the minimum resolution ( $1 \text{ km}^2$ ), the rebuilding algorithm seems to provide very accurate rain fields as soon as the resolution is set to less than  $4 \text{ km}^2$ . However, both the small size of the studied areas and the small number of rain events presented here require that more experiments be carried out to statistically confirm these conclusions.

Moreover, point-to-point comparisons are naturally less satisfactory in the large assimilation area (due to the model errors) but note the following characteristics:

- (i) The covered area can be much larger, provided the actual rainfall propagation can be described by an advection model. For instance, results are very good in both assimilation areas for the 20 October events.

- (ii) The model performance and the surface area covered can be increased by using more than one receiver.

## 2) RAIN GAUGE COMPARISON

The rain gauge data are point scale in space and time integrated (5-min resolution). To compare these data with the rainfall fields rebuilt from microwave measurements, the Ku rainfalls must be integrated over 5-min time periods and rain gauges must be assumed to provide good estimates of the rain fallen within the  $0.5\text{ km} \times 0.5\text{ km}$  cells of the assimilation algorithm, where the rain gauges are located. Figure 12 shows, for the four events studied, the cumulative rainfall measured by one of these rain gauges, located at Le Pradel (rain gauge 5, black dashed lines). The cumulative rainfalls measured by the Météo-France radar of Bollène on the  $1\text{ km}^2$  pixel, where the rain gauge is located, are also plotted (gray solid lines). There are significant differences between the total radar and rain gauge rainfall values—for instance, for the 20 October event, approximately 11.5 mm is recorded by the rain gauge and only 7 mm by the radar. However, note that the correlation coefficient between the data of the two rain gauges located near Le Pradel (rain gauges 5 and 6; see Fig. 2) is 0.97. The distance between these rain gauges is 415 m, which is close to the size of the grid boxes of our rebuilding algorithm. Figure 12 also shows the cumulative rainfalls at Le Pradel as reproduced by the algorithm (black solid lines). It should be noted that the microwave rainfall seems to be satisfactory: for all four events, the microwave rainfall values are closer to the rain gauge values than those provided by the radar. Therefore, the algorithm appears to provide a good assessment of the total rain fallen at particular ground points.

Another way to assess the performance of the algorithm on point-scale locations is to calculate the correlation coefficient between Ku and rain gauges data. Table 5 (third column) shows the correlation coefficients and the regression line equations between rain gauges and Ku rainfalls for different integration times, from 5 to 25 min. The data used are the values obtained for the four advective events and at the locations of the seven rain gauges within the large assimilation area (our algorithm cannot be used to estimate rainfall over rain gauges 1, 2, and 4, as seen in Fig. 2).

The Ku-link algorithm slightly underestimates the mean rain rate (the bias is  $-3.8\text{ mm h}^{-1}$  compared with the average rain gauge rain rate of  $24.5\text{ mm h}^{-1}$ ). Moreover, the radar also underestimates the point-scale mean rain rate but with a smaller difference ( $-1.9\text{ mm h}^{-1}$ ). The reasons for this underestimation is difficult to

elucidate (with only four events), although these results are consistent with Table 4, which shows that the Ku links slightly underestimate the mean rain rates in comparison with those derived from radar data for three out of four events.

For an integration time of 5 min, the correlation coefficient is rather small (0.63) and the slope of the regression line is also small (0.50). This confirms the tendency of our algorithm to smooth the rain fields, which is more pronounced because we compare space-integrated (microwave) and point-scale (rain gauges) data. A time scale is then sought at which a better fit between the two kinds of data would be obtained (by integrating the data over longer time periods). The correlation coefficients between Ku and rain gauge data are 0.76 and 0.77 at 10 and 15 min, respectively, while the slope of the regression lines are 0.63 and 0.62, respectively. Thus, the algorithm seems to lead to good results on point-scale locations for integration times larger than 10 min. For longer times, the correlation coefficient does not significantly increase (0.82 for 25 min). It should be noted that the correlation coefficients between radar and rain gauge data (Table 5, right column) are in good agreement, ranging from 0.69 for a 5-min integration time to 0.79 for 10 min and 0.84 for 25 min. This similarity between radar gauges and satlink gauges is likely because the measurements compared are of a different nature. Radar and Ku data are spatially integrated. When they are compared with point-scale data (rain gauges), the obtained regression slopes are substantially smaller than 1.

## 7. Conclusions

The use of a 4DVAR data assimilation algorithm allows certain local rain fields to be rebuilt from space-integrated rainfall data recorded by a very sparse network of Ku-band satellite-to-Earth microwave links. We produce local rainfall fields with a 10-s temporal resolution and a  $0.5\text{ km} \times 0.5\text{ km}$  spatial resolution, with features similar to those detected on radar maps having a temporal resolution of 5 min and a spatial resolution of  $1\text{ km}^2$ .

By working first on simulated data, we evaluate some of the consequences of the recording device's geometry on the results, including the algorithm's difficulty in reproducing northward advected events. We also note the difficulties resulting from numerical diffusion of the advection model used to propagate the rain fields through time. This numerical diffusion tends to smooth the rain fields after a small number of iterations over time and, on the contrary, to allow the algorithm to produce excessively strong gradients on the initial rain

fields, despite the addition of a filter term to the assimilation algorithm's cost function. These effects were also observed on real data recorded in the southeastern area of France in 2013. By comparing rebuilt fields with radar maps and point-scale rain gauge data, the algorithm generally obtains good results in the area directly below the Ku links, with a very satisfactory reproduction of the average rain rate in particular. However, we note that the performance of the model depends strongly on the realism of the advection scheme used to model rain field propagation in time and space. In a mountainous area such as the Cévennes–Vivarais region studied in this paper, the propagation of rain events cannot be reduced to a pure translation for more than a short period of time. We therefore worked with short events only (less than 45 min), selected according to their advective characteristics. The rebuilt areas (the small and large assimilation areas mentioned above) are thus quite small. However, a higher proportion of observed events (and the analysis of larger areas) could be correctly processed through the use of several Ku receivers. Moreover, it is shown that the use of two receivers allows the advection velocity to be determined using attenuation time series only.

Our results have been validated by comparing them with radar maps and rain gauge data. In cases where rain gauge data are available, it would be straightforward to adapt this algorithm to the assimilation of both microwave and rain gauge data (data fusion). A data fusion experiment (involving radar, rain gauge, and microwave link data) has been proposed by Bianchi et al. (2013). The addition of point-scale data (such as that provided by rain gauges) to spatially integrated data could enable the extrema, shapes, and characteristics of the rain fields to be more accurately determined.

In the present study, rain is assumed to fall vertically, and the attenuation determined with the Ku sensor is projected orthogonally onto the ground. A further improvement in the rebuilding algorithm could be achieved by taking into account the drops' horizontal displacements, produced by the wind field during their fall.

A further improvement in the algorithm's numerical ability to minimize the cost function, and to physically constrain the resulting rain fields, could be achieved by replacing the filter term of the cost function—for example, by including additional constraints on the rain field features, derived from their known meteorological characteristics.

Finally, it is interesting to note that the method described in this study could be a credible alternative to the use of radars for the observation of unmonitored zones (e.g., mountainous catchment areas, or the countryside

of developing countries). In the long term, rain monitoring networks could be set up in urban areas, through the addition of a small dedicated device to existing home TV satellite antennas.

*Acknowledgments.* This work was supported by the French Programme National de Télédétection Spatiale (PNTS, <http://www.insu.cnrs.fr/pnts>) Grant PNTS-2013-01 and by the Institut Pierre-Simon Laplace (IPSL). The authors wish to thank Drs. G. Molinié and B. Boudevillain from the Laboratoire d'étude des Transferts en Hydrologie et Environnement for supplying us with the HPiconet data.

#### REFERENCES

- Allen, D. J., A. R. Douglass, R. B. Rood, and P. D. Guthrie, 1991: Application of a monotonic upstream-biased transport scheme to three-dimensional constituent transport calculations. *Mon. Wea. Rev.*, **119**, 2456–2464, doi:10.1175/1520-0493(1991)119<2456:AOAMUB>2.0.CO;2.
- Barthès, L., and C. Mallet, 2013: Rainfall measurement from opportunistic use of earth-space link in Ku Band. *Atmos. Measur. Tech. Discuss.*, **6**, 2113–2150, doi:10.5194/amtd-6-2113-2013.
- Bianchi, B., P. Jan van Leeuwen, R. J. Hogan, and A. Berne, 2013: A variational approach to retrieve rain rate by combining information from rain gauges, radars, and microwave links. *J. Hydrometeorol.*, **14**, 1897–1909, doi:10.1175/JHM-D-12-094.1.
- Chwala, C., and Coauthors, 2012: Precipitation observation using microwave backhaul links in the alpine and pre-alpine region of southern Germany. *Hydrol. Earth Syst. Sci.*, **16**, 2647–2661, doi:10.5194/hess-16-2647-2012.
- Delrieu, G., B. Boudevillain, J. Nicol, B. Chapon, P.-E. Kirstetter, H. Andrieu, and D. Faure, 2009: Bollène-2002 Experiment: Radar quantitative precipitation estimation in the Cévennes–Vivarais region, France. *J. Appl. Meteor. Climatol.*, **48**, 1422–1447, doi:10.1175/2008JAMC1987.1.
- Desa, M., and J. Niemczynowicz, 1997: Dynamics of short rainfall storms in a small scale urban area in Coly Limper, Malaysia. *Atmos. Res.*, **44**, 293–315, doi:10.1016/S0169-8095(97)00017-3.
- Drobinski, P., and Coauthors, 2013: HyMeX, le cycle de l'eau méditerranéen à la loupe. *Meteorologie*, **80**, 23–36, doi:10.4267/2042/48792.
- Gilbert, J. C., and C. Lemaréchal, 2006: The module M1QN3. INRIA Rep., version 3.3, 21 pp.
- Giuli, D., A. Toccafondi, G. Biffi Gentili, and A. Freni, 1991: Tomographic reconstruction of rainfall fields through microwave attenuation measurements. *J. Appl. Meteor.*, **30**, 1323–1340, doi:10.1175/1520-0450(1991)030<1323:TRORFT>2.0.CO;2.
- , L. Facheris, and S. Tanelli, 1999: Microwave tomographic inversion technique based on stochastic approach for rainfall fields monitoring. *IEEE Trans. Geosci. Remote Sens.*, **37**, 2536–2555, doi:10.1109/36.789649.
- Kalnay, E., 2003: *Atmospheric Modeling, Data Assimilation, and Predictability*. Cambridge University Press, 364 pp.
- Leijnse, H., R. Uijlenhoet, and J. Stricker, 2008: Microwave link rainfall estimation: Effects of link length and frequency, temporal sampling, power resolution, and wet antenna attenuation. *Adv. Water Resour.*, **31**, 1481–1493, doi:10.1016/j.advwatres.2008.03.004.

- Lovejoy, S., and D. Schertzer, 1990: Multifractals, universality classes and satellite and radar measurements of cloud and rain fields. *J. Geophys. Res.*, **95**, 2021–2034, doi:10.1029/JD095iD03p02021.
- Maitra, A., and K. Chakravarty, 2005: Ku-band rain attenuation observations on an earth–space path in the Indian region. *Proc. XXVIIIth General Assembly, URSI, New Delhi, India, F01.4(0650)*. [Available online at <http://www.ursi.org/Proceedings/ProcGA05/pdf/F01.4%280650%29.pdf>.]
- Molinié, G., D. Ceresetti, S. Anquetin, J. D. Creutin, and B. Boudevillain, 2012: Rainfall regime of a mountainous Mediterranean region: Statistical analysis at short time steps. *J. Appl. Meteor. Climatol.*, **51**, 429–448, doi:10.1175/2011JAMC2691.1.
- Nardi, L., C. Sorrow, F. Badran, and S. Thiria, 2009: YAO: A software for variational data assimilation using numerical models. *Computational Science and Its Applications—ICCSA 2009*, O. Gervasi et al. Eds., Lecture Notes in Computer Science, Vol. 5593, 621–636.
- Navon, I. M., 2009: Data assimilation for numerical weather prediction: A review. *Data Assimilation for Atmospheric, Oceanic and Hydrologic Applications*, S. K. Park and L. Xu, Eds., Vol. 1, Springer, 21–65.
- Overeem, A., H. Leijnse, and R. Uijlenhoet, 2013: Country-wide rainfall maps from cellular communication networks. *Proc. Natl. Acad. Sci. USA*, **110**, 2741–2745, doi:10.1073/pnas.1217961110.
- Schleiss, M., and A. Berne, 2010: Identification of dry and rainy periods using telecommunication microwave links. *IEEE Geosci. Remote Sens. Lett.*, **7**, 611–615, doi:10.1109/LGRS.2010.2043052.
- Smolarkiewicz, P. K., 1983: A simple positive definite advection scheme with small implicit diffusion. *Mon. Wea. Rev.*, **111**, 479–486, doi:10.1175/1520-0493(1983)111<0479:ASPDAS>2.0.CO;2.
- Tabary, P., 2007: The new French operational radar rainfall product. Part I: Methodology. *Wea. Forecasting*, **22**, 393–408, doi:10.1175/WAF1004.1.
- Thiria, S., F. Badran, and C. Sorrow, 2006: Yao: Un logiciel pour les modèles numériques et l'assimilation de données. LOCEAN Research Rep., 60 pp.
- Verrier, S., L. De Montera, L. Barthès, and C. Mallet, 2010: Multifractal analysis of African monsoon rain fields, taking into account the zero rain-rate problem. *J. Hydrol.*, **389**, 111–120, doi:10.1016/j.jhydrol.2010.05.035.
- Zinevich, A., P. Alpert, and H. Messer, 2008: Estimation of rainfall fields using commercial microwave communication networks of variable density. *Adv. Water Resour.*, **31**, 1470–1480, doi:10.1016/j.advwatres.2008.03.003.
- , H. Messer, and P. Alpert, 2009: Frontal rainfall observation by a commercial microwave communication network. *J. Appl. Meteor. Climatol.*, **48**, 1317–1334, doi:10.1175/2008JAMC2014.1.